Chapter 3

Tailoring the Electronic and Magnetic Properties of Peculiar Triplet Ground State Polybenzoid “Triangulene”

3.1 Introduction

Graphene is known to be the center of attraction since the last decade due to its exceptional properties making it a potential nanomaterial for wide range of applications like in chemical sensors, organic semiconductors, composite materials, biological engineering, photovoltaic cells, energy storage devices, spintronics etc. [1–3]. Apart from its fascinating properties, absence of electronic band gap restricts it from direct application in electronics which is its major limitation. Many strategies have been utilized for the band gap opening in graphene like controlling its size, doping heteroatom and by creating defects [4]. Another method to tailor the electronic properties is quantum confinement. The graphene quantum dots (GQDs) are the nanometer-scaled graphene flakes which consists similar sp^2 hybridized carbon bonds. Presently GQDs are mainly utilized in photoluminescence (PL) and in display screen manufacturing [5–6]. The GQDs are small flakes of graphene with zero-dimensionality (0D) which contains properties of both graphene as well as carbon dots (CDs) [7–8]. GQDs containing quantum confinement and edge effects make them superior from organic dyes and semiconducting quantum dots (SQDs) in terms of low toxicity, biocompatibility, and high photostability [7–9]. The polycyclic aromatic hydrocarbon (PAH) units are present in small fragments known as nanographene which is generated from graphene [10–11]. Various characteristics like intense spin open-shell radical property in ground-state are observed in these nanographenes [11]. There are few examples, like phenalenyl [12] which comprises odd number of π electrons due to odd carbon atoms resulting in its neutral ground state. The triangularly extended benzene ring structure which leads to several derivatives containing π-conjugated phenalenyl such as Clar's hydrocarbon commonly known as triangulene is another example. Triangulene which is an obscure molecule (known as smallest triplet-ground-state polybenzoid), have di-radicals and contains 22 carbon atoms with the fused benzene rings, gather much attention ever since it was first hypothesized [13]. The presence of two unpaired valence electrons restricts the possibility of Kekulé structure in the whole molecule. The system contains even number of π-electrons, however there is limitation in resonance structure where each π-electron is paired with nearby carbon [14]. Due to the intense reactivity and synthesis process of triangulene, its standalone form was not attained [13]. It was observed currently that the manipulation of pyrene obtained from solution of pyrene isomers over Cu (111), NaCl (100) and Xe (111) surfaces leads to formation of triangulene [15]. The study

reveals that the triangulene accumulates characteristics of free molecule on outer layer with 3-fold symmetry which is confirmed by STM, DFT and AFM calculations [15]. Triangulene shows magnetic properties which arises due to aligned spins and provides magnetic orientation of two unpaired electrons. This peculiar magnetic property makes pathway for triangulene to be utilized in spintronics, quantum information processing (QIP), electronics, and quantum computing [16–17]. The analysis of triangulene on sodium chloride, copper and xenon surface through DFT reveals its extensive molecular properties [15]. However, the fundamental understandings of ground-state along with its excited states which will contribute in tuning the properties of distinct triangulene are still lacking. Thus, with this motivation, a systematic study on graphene quantum dots, triangulene is conducted using the DFT based on first principles calculations. Open shell or unpaired electrons in triangulene and its derivative results in the magnetism which makes their strong application towards the spintronics [16]. Recently, the area of spintronics exhibits the significant gain due to the use of spin of electron as transport of information instead of charges. The magnetic ordering due to strong diamagnetic nature is observed in graphene. Many approaches like vacancy or defect creation [18-20], addition of heavy, light as well as transition metal elements [21-23] and the functionalization of edges [24] have been utilized in order to understand the change of magnetic moment in graphene using both theoretical and experimental techniques. Moreover, the quantum confinement in graphene leads to the GQDs which further tunes the diamagnetic nature of graphene [25]. In GQDs, the charge carriers are restricted in all three spatial directions making it easy to control individual electron, supporting to investigate the behavior of spins [26]. Literature survey reveals a lack in the understanding of magnetic interactions in triangulene. Therefore, we have systematically studied the magnetic properties of pristine and iron (Fe), cobalt (Co), nickel (Ni), and copper (Cu) doped triangulene [27]. The aim of the present work is threefold (i) to analyze the ground state electronic and vibrational characteristics of triangulene, (ii) to study magnetic states of triangulene by doping of transition metal elements and (iii) to analyze various global reactivity descriptors like electrophilicity, global hardness, polarizability, and charge transfer in triangulene [27].

3.2 Computational methods

Ground state optimization, electronic energy states i.e. density of states (DOS) and vibrational frequency calculations were carried out by adopting the open-shell Becke's three parameter (B3) having the hybrid functional of Lee–Yang–Parr (LYP) exchange–correlation potential (B3LYP) [28] along with the basis set 6–31G in Gaussian 09 suite of program [29]. The reason for choosing the open-shell B3LYP is that it is more stable than closed shell for dibenzoterrylene-acenes hybrids [30]. There is absence of any external field during full structure relaxation. We have also calculated the Raman intensities and the vibrational frequencies of triangulene. All obtained results and the structure like pictorial visualization, checking of calculated data, molecular orbitals, Raman, IR spectra and the representation of isoelectronic molecular electrostatic potential surfaces (MESP) is visualized by GaussView [31] program. Difference between the highest occupied molecular orbital (HOMO) energy and lowest unoccupied molecular orbital (LUMO) energy was used to find the energy gap, i.e. $E_g = E_{LUMO} - E_{HOMO}$. The chemical reactivity of a triangulene was also calculated which is shown by global electronic reactivity descriptors. Moreover, the global reactivity descriptors such as electronegativity (χ), chemical potential (μ), global hardness (η), global electrophilicity index (ω) and global softness (S) were calculated yielding through Koopman's theorem [28], from the E_{LUMO} and E_{HOMO} and are presented by following equations [32-33]:

$$\boldsymbol{\chi} = -\frac{\mathbf{1}}{\mathbf{2}}\left(\mathbf{E}_{\boldsymbol{HOMO}} + \mathbf{E}_{\boldsymbol{LUMO}}\right) \tag{3.1}$$

$$\boldsymbol{\mu} = -\boldsymbol{\chi} = \frac{\mathbf{1}}{\mathbf{2}}\left(\mathbf{E}_{\boldsymbol{HOMO}} + \mathbf{E}_{\boldsymbol{LUMO}}\right) \tag{3.2}$$

$$\boldsymbol{\eta} = \frac{\mathbf{1}}{\mathbf{2}}\left(\mathbf{E}_{\boldsymbol{LUMO}} - \mathbf{E}_{\boldsymbol{HOMO}}\right) \tag{3.3}$$

$$\boldsymbol{S} = \frac{\mathbf{1}}{\mathbf{2}\boldsymbol{\eta}} \tag{3.4}$$

$$\boldsymbol{\omega} = \frac{\boldsymbol{\mu}^{\mathbf{2}}}{\mathbf{2}\boldsymbol{\eta}} \tag{3.5}$$

$$\boldsymbol{\Delta N_{max}} = -\frac{\boldsymbol{\mu}}{\boldsymbol{\eta}} \tag{3.6}$$

Furthermore, the nature of interaction between the triangulene and transition metal elements was studied by calculating the adsorption energy (ΔE_{ad}) using the following expression:

$$(\Delta \boldsymbol{E_{ad}}) = \boldsymbol{E_{triangulene+Fe/Co/Ni/Cu}} - \left(\boldsymbol{E_{triangulene}} + \boldsymbol{E_{Fe/Co/Ni/Cu}}\right) \quad (3.7)$$

Where $E_{\text{triangulene+Fe/Co/Ni/Cu}}$ represents the total energy of combined system of triangulene and transition metals. $E_{triangulene}$ and $E_{\text{Fe/Co/Ni/Cu}}$ are the individual total energy of triangulene and transition metal elements, respectively. The calculated ΔE_{ad} for all the considered systems was corrected by removing basis function overlap effects using basis set superposition error (BSSE) [34].

3.3 Results and Discussion

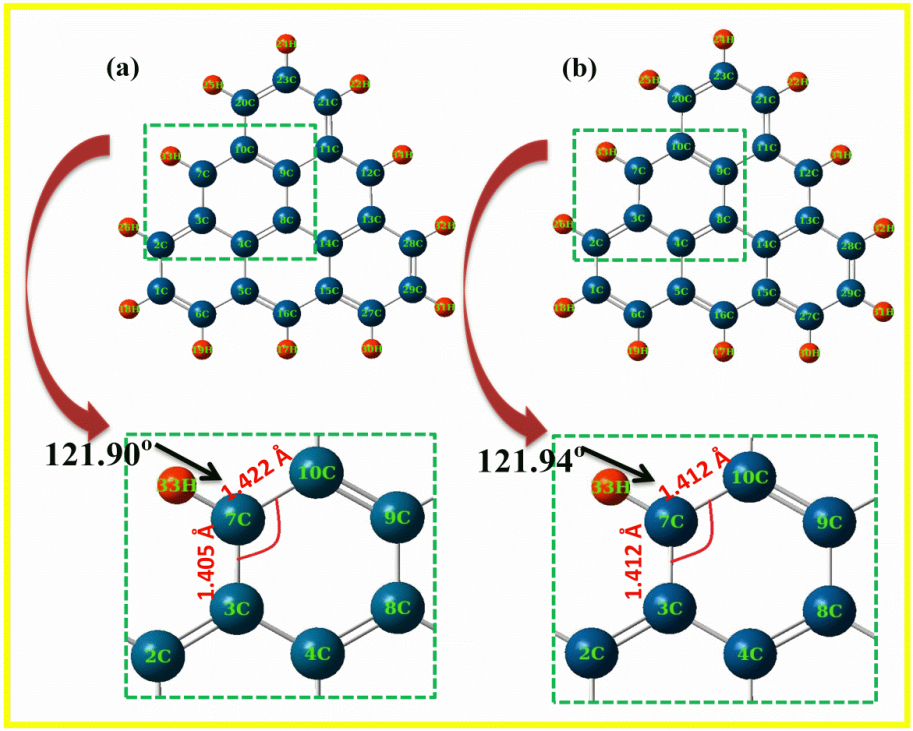

Figure 3.1: Ground state geometries of triangulene with (a) Antiferromagnetic (AFM) (b) Ferromagnetic (FM) structure with atomic numbering scheme. The carbon and hydrogen atoms respectively are determined by the blue and red spheres.

For the investigation of properties mentioned above, we used basic structure of triangulene recently reported by Pavliček et al. [15]. The Figs. 3.1 (a) and (b) presents the optimized

geometries of triangulene with the anti-ferromagnetic (AFM) singlet and ferromagnetic (FM) triplet states. Both the singlet and triplet state structures exhibit the different bond length, which are visible in the enlarged inset section. The bond length of 1.412 Å is obtained for 10C-7C and 7C-3C pair of carbon atoms in triplet state presenting its more stability than the singlet state which exhibits the diverse bond lengths of magnitude 1.422 Å and 1.40 Å for same carbon atoms. The reason for this difference could be the ferromagnetic minimum energy structure and also shapes and edges of the structure which relies on the geometrical parameters such as bond lengths and angles in the ring of benzene structure, further modifying the magnetic properties of triangulene like other GQDs [35-37].

Figure 3.2 shows the optimized geometries of transition metal Fe, Co, Ni and Cu doped triangulene. DFT calculations were performed by putting the transition metal atoms on the top-site of carbon atom named as 8C in triangulene having gap of 1.8 Å between them.

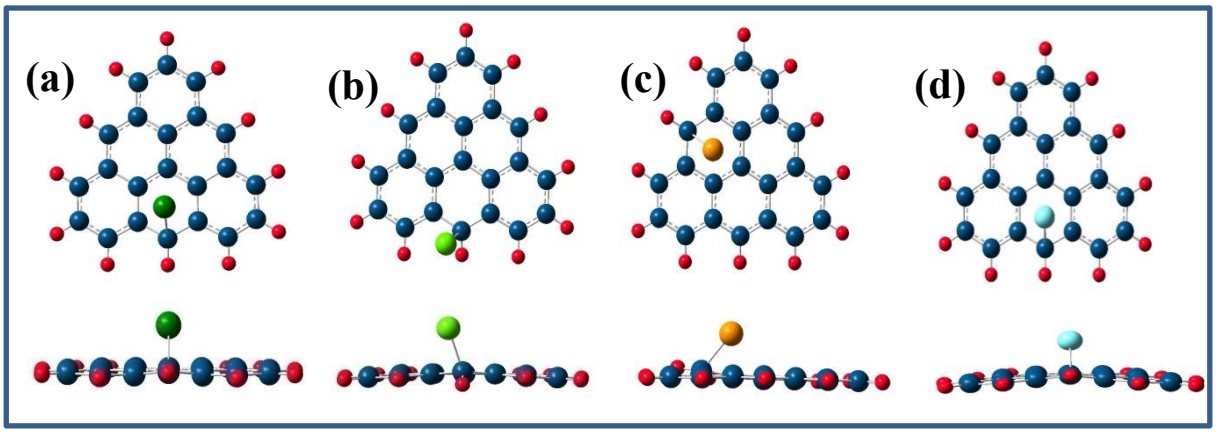

Figure 3.2: Optimized geometries of triangulene with (a) Iron (b) Cobalt (c) Nickel and (d) Copper adatoms along with top and side view. The green, fluorescent, orange, and light blue balls represent iron, cobalt, nickel and copper atoms respectively.

Geometry calculations reveal the self-reorientation of transition metals at the external of triangulene. It might be due to the excess of electropositive nature on the outer side of triangulene and the highly electronegative exhibited by considered transition metal elements. Here, bond length increases up to 1.95 Å, 1.91 Å, 2.05 Å for Fe, Co and Cu and shift towards the 16C carbon atom having the bond angle of 130˚, 100˚ and 125˚ for 17H-16C-35Fe/Co/Cu,

respectively. However, Ni dragged along the unpaired electron located at 7C atom and exhibits the bond length of 1.94 Å and bond angle 33H-7C-35Ni of 127.5˚.

Table 3.1 depicts the obtained total energy and dipole moments of pristine as well as transition metals doped triangulene with AFM and FM structures. From the energy calculation, we observe that the FM state of triangulene exhibits more stability as compared to AFM singlet state, which are in accordance with the previous report [15]. Additionally, we have also studied two different FM phases (alpha and beta) of triangulene due to its energetically stable nature, which basically determines the up and down orientation of spin orbitals in FM materials. Due to the peculiar electronic nature of triangulene which arises from two unpaired electrons, it reveals both alpha (+1/2) and beta (-1/2) spin states. Table 3.1 clearly predicts the adsorption of transition metal elements on triangulene leading to the enhancement of dipole moment compared to pristine triangulene. The information regarding the change in excitation due to the electronic distribution is retrieved from the dipole moment of the molecule. Significant increment in total energy is observed after the adsorption of considered transition metal elements which leads triangulene structure towards more stability.

Table 3.1: The ground state energy and calculated dipole moment for pristine and doped triangulene.

Triangulene	Energy (eV)	Dipole Moment (Debye)
Antiferromagnetic (AFM)	-23004.41	0.0325
Ferromagnetic (FM)	-23005.05	0.0002
Triangulene+Fe	-57369.76	3.266
Triangulene+Co	-60611.14	3.355
Triangulene+Ni	-64026.12	1.727
Triangulene+Cu	-67620.42	2.244

The FM and AFM states of triangulene show the dipole moments of 0.0002 and 0.0325 Debye respectively. It is observed that lone pair electrons for the molecular displacement show the considerable participation in higher value of dipole moment instead of the covalently bonded electrons. The AFM state of triangulene significantly reveals the higher value of dipole moment leading to high reactivity and less stability than FM state of triangulene, which is supported by

the energy shown in Table 3.1. The net dipole moment is zero as the dipole moment of the bonds cancel out each other for high symmetrical molecules. Another reason for zero dipole moment is the opposite spins of the electron pair resulting in opposite directions of their magnetic dipole fields. But in case of an unpaired electron there will be interacting magnetic fields having the magnetic dipole. Thus, in triangulene, the unique molecular structure is responsible for the presence of two unpaired electrons, which further restrict the cancellation of the dipole moments. Consequently, this will be similar for all such molecules having similar geometries resulting in non-zero dipole moment [38].

Table 3.2: Calculated energies of HOMO-LUMO, HOMO-LUMO gap (E_g), adsorption energy (E_{ad}) and magnetic moment (M) of all considered systems.

System	E_{HOMO} (eV)	E_{LUMO} (eV)	E_g (eV)	E_{ad} (eV)	M(μB)
Triangulene + Fe	-12.8	-10.09	2.7	-11.7	4.8
Triangulene + Co	-13.3	-9.80	3.5	-9.77	4.82
Triangulene + Ni	-12.86	-10.03	2.83	-10.5	4.85
Triangulene + Cu	-10.57	-9.28	1.28	-17.58	4.857

The adsorption energies of transition metal elements over the triangulene are shown in Table 3.2, which are much larger for triangulene as compared to graphene, CNT, bilayer graphene and MoS_2 [21,39-41]. After the optimization, all considered transition metal elements are covalently bonded with triangulene which leads to the chemisorption (Fig. 3.2). According to the Table 3.2, the strength of the transition metal adsorption over triangulene follows Cu > Fe > Ni > Co order. Further, we have also calculated the magnetic moment, as these transition metals, gives rise to the magnetic moment in triangulene. From the DFT calculations, we obtain the atomic magnetization M for stable spin states. Table 3.2 presents absolute values of magnetic moments after adsorption of transition metals. The FM phase of triangulene exhibits $4.23\mu_B$ atomic magnetization due to unpaired electron which is rather higher. With the adsorption of transition metal elements over the triangulene, magnetic moments are slightly increased. In all considered systems, increment in the magnetic moment of ~0.62 μ_B is observed which is larger as compared to others [21,41-43].

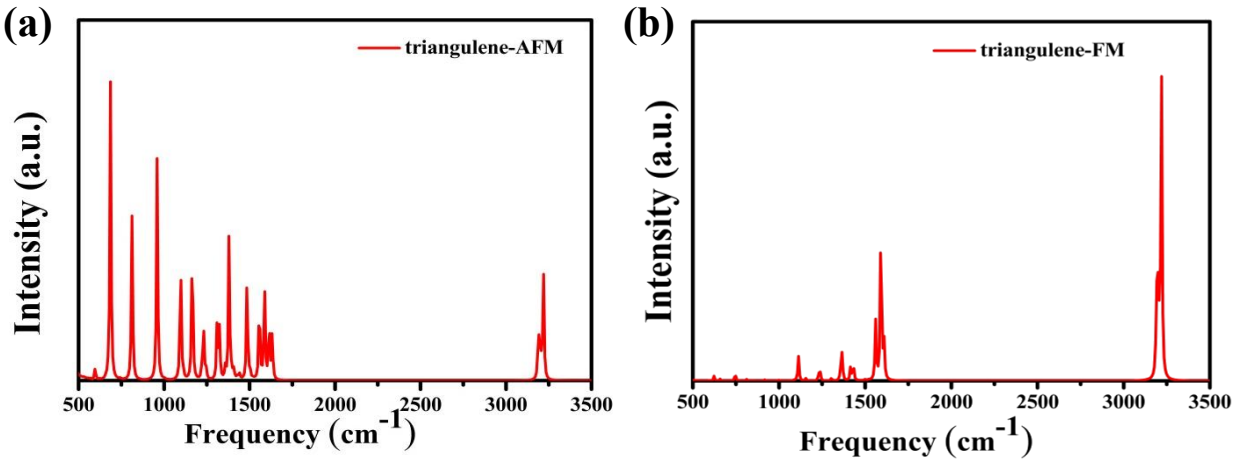

Figure 3.3: Raman spectra of both (a) AFM (b) FM phases of triangulene.

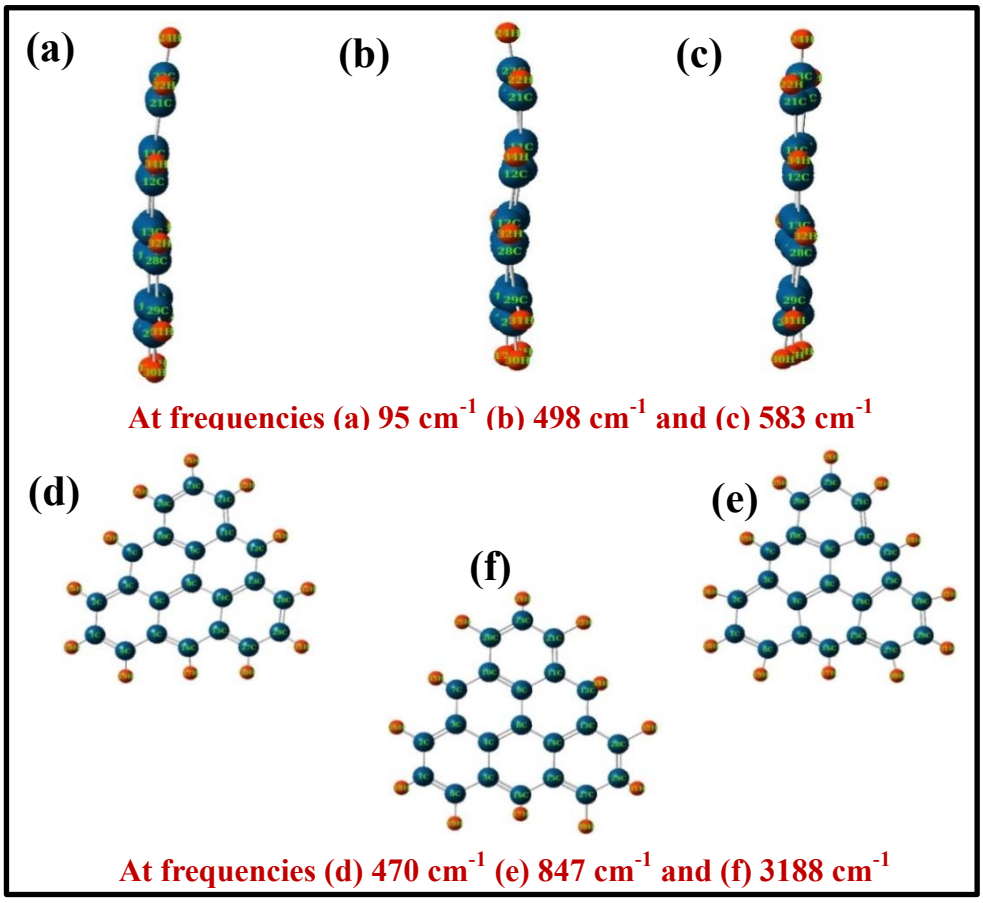

Figure 3.4: Several Raman and IR molecular vibrations of triangulene. (a-c) presents the out-of-plane vibrations and (d-e) presents in-plane vibrations.

Figure 3.3 presents the Raman spectra, plotted against harmonic vibrational wavenumbers. We can see from the figure that both AFM and FM magnetic phases of triangulene consists real frequencies only, which suggests the local stability of both magnetic structures.

Table 3.3: Raman and IR vibrational assignments for FM and AFM phases of triangulene.

Triplet States (FM)		Singlet States (AFM)	
Cal. IR/Raman Bands	**Representation**	**Cal. IR/Raman Bands**	**Representation**
84^{R}	**(20C=23C-21C), (27C-29C-31H), (10C=9C-11C), (4C=8C-14C), (4C=8C-9C), (14C-8C-9C), (10C-20C=23C), (4C-3C-7C), (14C=13C-12C) s stretching**	**138179^{R}**	**(10C-20C=23C), 23C-21C=11C), (10C=9C-11C), (2C=3C-7C), (12C-13C-28C), (5C=16C-15C), (4C=8C-14C) a. s. stretching**
72^{IR}	**(2C-26H)+(1C-18H)+ (6C-19H)+ (27C-30H)+ (29C-31H)+ (28C-32H)+(21C-22H) wag o.p**	**9590^{R}**	**(10C-20C)+ (11C-21C) rocking i.p**
130^{IR}	**(3C-7C-33H), (13C-12C-34H), (1C-18H), (29C-31H) wag o.p**	**153^{IR}**	**(21C-22H), (20C-25H), (10C=9C-11C) twisting o.p**
60^{R}	**(20C=23C-21C) a.s stretching, (15C-14C=13C) (3C-7C-10C), (1C-2C=3C) s. stretching, (20C-25H), (21C-22H) rocking i.p**	**2461^{IR}**	**All rings i.p rocking + ring deformation**
27^{R}	**(10C=9C-11C) scissoring i.p (20C=23C-21C), (4C=8C-14C) a.s stretching, (16C=5C-4C),(1C-2C=3C) scissoring i.p +ring deform**	**14^{IR}**	**(2C-26H)+(1C-18H)+ (6C-19H)+ (27C-30H)+ (29C-31H)+ (28C-32H)+(21C-22H) wag o.p**
18^{R}	**(4C=8C-14C), (20C=23C-21C), (10C=9C-11C)a.s stretching, (3C-7C-10C), (13C-12C-11C)s. stretching, (6C=1C-2C), (29C=28C13C) scissoring i.p + ring deform**	**2880^{R}**	**(20C=23C-21C), (23C-21C=11C), (3C-7C-10C), (11C-12C-13C) scissoring i.p**
25^{R}	**(9C-8C-14C) scissoring i.p, (26H-2C), (1C-18H), (6C-19H), (29C-31H), (28C-32H), (20C-25H), (21C-22H) rocking i.p**	**61^{IR}**	**(25H-20C=23C-24H), (24H-23C-21C-22H), (26H-2C-1C-18H), (30H-27C-29C-31H) wag o.p**
78^{R}	**(20C-25H), 23C-24H), 21C-22H) rocking i.p, (13C-12C-11C), (10C-7C-3C), (15C-16C=5C) s. stretching, (12C-(13C=14C), (7C-3C-4C), 27C=15C-16C), (16C=5C-6C) a.s stretching + ring deformation**	**107^{IR}**	**(25H-20C=23C-24H), (24H-23C-21C-22H), (26H-2C-1C-18H), (30H-27C-29C-31H) twisting o.p**
238^{R}	**(20C-25H), (21C-22H) rocking i.p, (2C=3C-4C), (14C=13C-28C), (2C-1C=6C), (27C-28C=29C)a.s stretching, (4C=8C-14C)s.stretching, (5C=16C-15C) + ring deform**	**2303^{R}**	**(10C-20C-25H), (11C=21C-22H), (27C-30H), (28C-32H), (6C-19H), (2C-26H) rocking i.p, (4C=8C-14C) scissoring i.p + ring deformation**
213^{R}	**(2C-26H), (20C-25H), (21C-22H), (6C-19H) s. stretching**	**672^{R}**	**(26H-2C), (6C-19H), (27C-30H), (28C-32H) rocking i.p, (5C=16C-15C), (10C=9C-11C) scissoring i.p**
81^{IR}	**(18H-1C-2C-26H), (31H-29C=28C-32H) a.s. stretching, (18H-1C=6C-19H), (30H-27C-29C-31H) s. stretching**	**976^{R}**	**(23C-24H), (12C-34H), (7C-33H), (16C-17H) rocking i.p, (10C=9C-11C), (4C=8C-14C), 3C-7C-10C), (11C-12C-13C) a.s. stretching**
1054^{R}	**(20C-25H), (23C-24H), (21C-22H), (2C-26H), (1C-18H), (28C-32H), (29C-31H), (6C-19H), (27C-30H) s. stretching**	**91^{IR}**	**(20C-25H), (23C-24H), (21C-22H), (2C-26H), (28C-32H), (29C-31H), (1C-18H) (6C-19H), (27C-30H) s. stretching**

All frequencies are in cm^{-1}. s, a.s, i.p and o.p shows symmetry, anti-symmetry, in-plane and out-of-plane vibrations.

As triangulene has carbon atoms, mainly like graphene, the G and D bands which are fingerprints of graphene are obtained nearby 1596 cm^{-1} and 1350 cm^{-1}, respectively for both FM and AFM phases. Stretching between two carbon atoms originates the G band and also exhibits the first order E_2g phonon mode at the zone center of the first Brillouin zone (BZ). D band is originated in both FM and AFM phases attributed to the presence of finite crystalline size. There is a localized mode around ≈3220 cm^{-1} observed due to typical C–H vibration in triangulene [44]. The analysis regarding the Raman and IR vibrational modes of pristine triangulene are systematically given in Table 3.3. Some of the weak bands of stretching vibrations related with C–C and C–H are found between 1000–3230 cm^{-1}. The C–H out-of-plane bending vibrations of triangulene (FM) are located at 72 cm^{-1} and 130 cm^{-1} in the infrared spectra. However, in the AFM phase of triangulene, peaks between 50–500 cm^{-1} in the Raman spectra are attributed to C=C, C–C and in-plane stretching cause ring deformation. The C–H, C=C with out-of-plane bending and in-plane stretching vibrations in the IR spectra are found at 107 cm^{-1} and 91 cm^{-1}. All the calculated values of the frequency along with vibrational assignments are shown in Table 3.3. The displacement of eigenvectors is shown in Fig. 3.4 and the distortion of triangulene benzoid rings can also be seen.

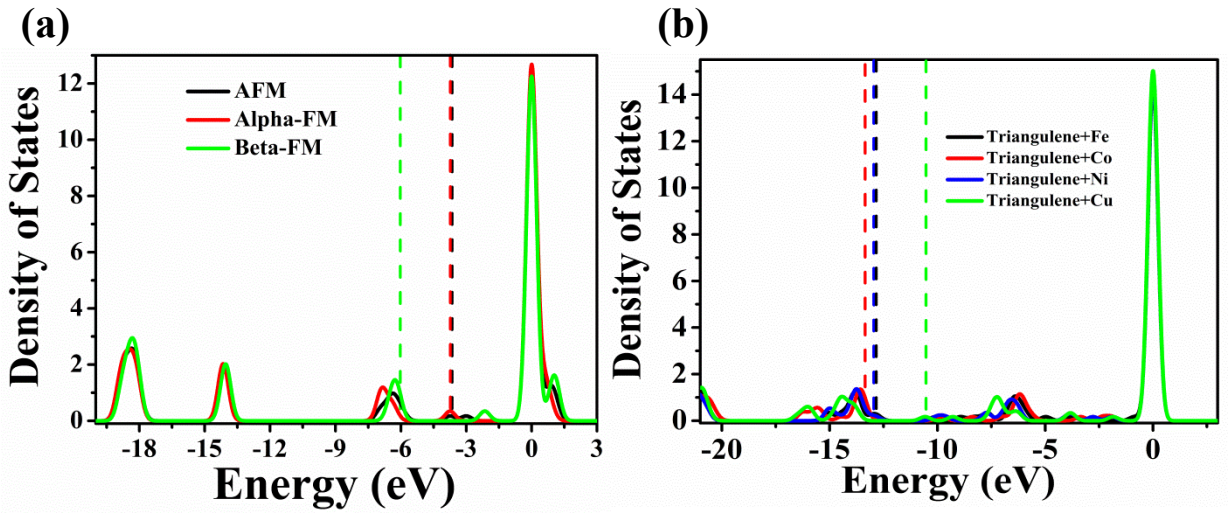

Figure 3.5: Electronic DOS for (a) AFM, alpha-FM and beta-FM phases of triangulene, and (b) transition metal elements adsorbed triangulene.

Figure 3.5(a) depicts the electronic DOS for AFM state along with alpha and beta orbitals. The DOS reflects the zero dimensional (0D) structural phenomena of triangulene due to discrete nature of electronic states determined by the delta function. The DOS for transition metal elements adsorbed over triangulene is presented in Fig. 3.5(b). HOMO energies in both the figures are denoted by the vertical dashed line. A clear shift of HOMO energy can be seen from the graph. The HOMO and LUMO energies level of both the magnetic phases of triangulene including alpha and beta spin configuration are shown in Fig. 3.6. The calculated E_g is 0.738 eV for AFM, 4.234 eV for FM-alpha and 3.968 eV for FM-beta configurations respectively. Conventionally, alpha and beta orbitals of FM state must exhibit the exact value of HOMO and LUMO, however, two unpaired electrons further, creates significant difference. AFM state possesses the lower band gap compared to the FM state. From the HOMO-LUMO gap, one can describe the electrical transport and chemical stability of triangulene. The high and low stability is reflected by large and small gaps respectively. Thus, the former discussion might reflect the more stable nature of FM state in triangulene.

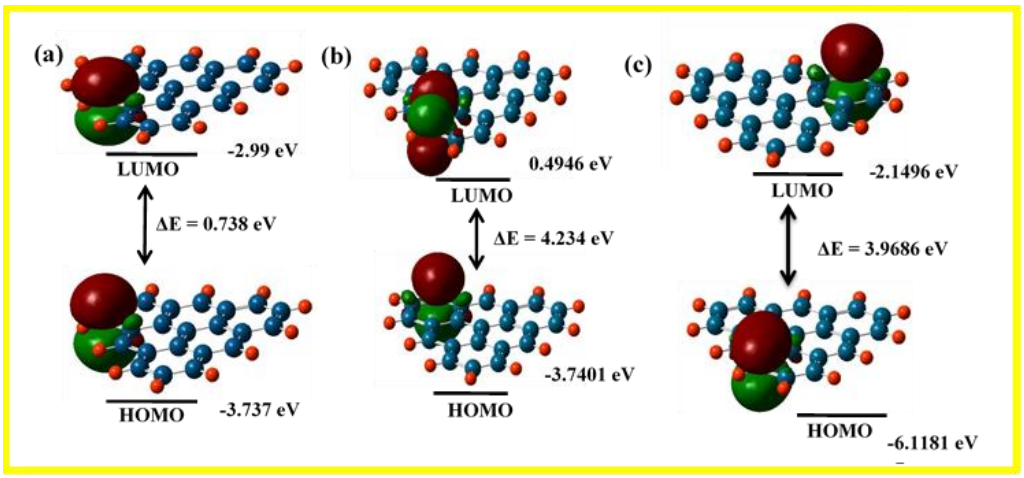

Figure 3.6: HOMO and LUMO levels of triangulene (a) AFM (b) alpha-FM (c) beta-FM.

Further, small HOMO-LUMO gap of molecule suggests its more polarizability (reactive) or instability, observed for triangulene with AFM state [45-46]. Frontier molecular orbitals for transition metal elements adsorbed triangulene are presented in Fig. 3.7 along with their energy gap between them. The anomalous fluctuation in E_g is observed as it increases from Fe to Co and

decreases from Co to Cu adatoms. This can be attributed to the inclusion of electrons further reducing the gap between HOMO and LUMO energy levels.

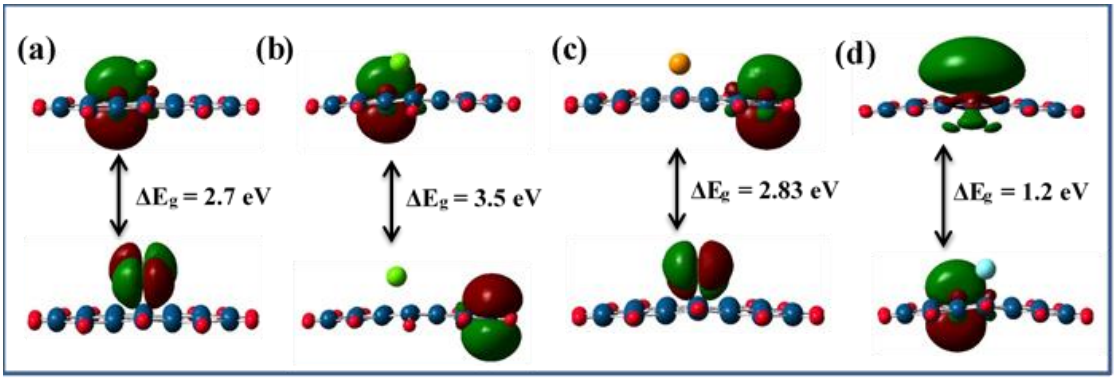

Figure 3.7: HOMO and LUMO levels of triangulene (a) Fe (b) Co (c) Ni and (d) Cu.

Moreover, the global reactivity parameters like η, S, ω, μ, and ΔN from the neighboring atoms evaluated using Koopmans' theorem are presented in Table 3.4. Here, the least value of η for AFM triangulene as compared to FM triangulene depicts the less stability of AFM phase.

Table 3.4: Calculated HOMO and LUMO energies (eV) along with global reactivity parameters.

Triangulene	**HOMO (eV)**	**LUMO (eV)**	**E_g (eV)**	**χ (eV)**	**μ (eV)**	**η (eV)**	**S (1/eV)**	**ω (eV)**	**ΔN_{max} (eV)**
Anti ferromagnetic	-3.7377	-2.9997	0.738	3.368	-3.368	0.369	-1.355	-15.37	-9.12
Alpha Ferromagnetic	-3.7401	0.4946	4.234	1.622	-1.622	2.117	-0.2361	-0.621	-0.76
Beta Ferromagnetic	-6.1182	-2.1496	3.968	4.133	-4.133	1.984	-0.2519	-4.305	-2.08

We found that the global hardness(η) for the beta FM phase is highest. When the additional charge is received from the adjacent atoms, the stability is given by the global electrophilicity index (ω). Further, electrophile charge transfer is governed through the chemical potential of the

electrons. Thus, acceptance of electrons leads to the negative value of chemical potential along with energy. The larger value of ω reveals that FM phase of triangulene exhibits the stronger electrophile nature than AFM. By theoretically deriving electron density one can calculate the molecular electrostatic potential (MESP) which is an essential measure for understanding the molecule's interactive behavior [47-48]. The intense negative features identified in topography of MESP V_{min} depict the fundamental understanding of electron donating properties. Further, the interactive behavior of the molecule for a specific atom having electron abundant and deficient site with additional molecule is determined by the MESP at a nucleus V_n. Thus, electronegativity can be predicted by the MESP, which is also useful to analyze the interacting site, partial charges and dipole moment. MESP at point r nearby molecule (in atomic units) can be given by,

$$\boldsymbol{V(r)} = \sum \frac{\boldsymbol{Z_A}}{\boldsymbol{|R_A - r|}} - \int \frac{\boldsymbol{\rho(r')\, dr'}}{\boldsymbol{|r' - r|}} \tag{3.8}$$

Where Z_A determines the charge on nucleus A having the position coordinate R_A and the charge density is $\rho(r')$ at any point *r*. On the right hand side of equation 3.8, the first terms depict the effect caused by the nuclei, while second term shows electronic contribution. $V(r)$ presents the effective electrostatic potential at any point *r*, due to both the electrons and nuclei.

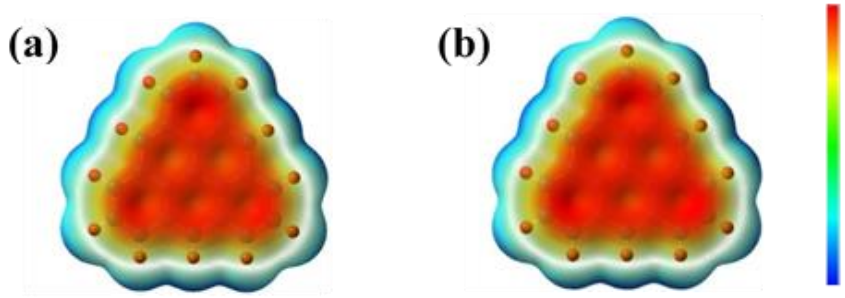

Figure 3.8: MESP plotted for (a) AFM triangulene ranging -2.102 x 10^{-2} (red) to + 2.102 x 10^{-2} (blue). (b) FM triangulene ranging -2.043 x 10^{-2} (red) to + 2.043 x 10^{-2} (blue).

Figure 3.8 presents MESP surfaces for both FM and AFM phases of triangulene. The most negative and positive electrostatic potential are determined by red and blue colors, respectively, while the green color in Fig. 3.8 depicts the surface zero potential. Moreover, the positive MESP surfaces reveal the repulsive nature of proton and atomic nuclei in low density field and also tells us that the nuclear is incompletely guarded, while, the attraction of proton by the concentrated electron density in the molecule is shown by negative MESP. The MESP at distinct points on the iso-surface of electron density is depicted through the color of iso-surface contours. These increment in the potential is in the sequence of red < orange < yellow < green < blue.

3.4 Conclusions

Being experimentally ambiguous, triangulene has stand out as relevant GQD for its theoretical calculations and analysis. The characteristic which makes triangulene different is its two π-electrons which are difficult to be paired resulting in two different orientations: antiferromagnetic singlet state and ferromagnetic triplet state. The systematic DFT investigation of pristine triangulene, considering the two spin orientation, exhibits the most stable state in the ferromagnetic orientation instead of antiferromagnetic order. This is further confirmed by calculating energies and global reactivity descriptors acquired from Koopmans' theorem. For the stable FM state of triangulene, higher energy gap between HOMO and LUMO energy levels and global hardness is observed. The stability of triangulene was further confirmed by vibrational frequencies calculation which suggests real frequencies. The discrete nature of the energy states in DOS reveals the confinement in all the three spatial dimensions, further validates the triangulene GQD. The large magnetization of triangulene makes it a useful material for spintronic device applications. Significant modification in magnetic moment is observed after adsorption of adatoms such as iron, cobalt, nickel and copper over the triangulene, which contributes increase in ground states in high-spin state, suggesting its potential applications in organic spintronic devices. The study suggests that interesting magnetic behavior can be formed by varying the adatoms concentration to make a magnetic island.

Reference

1. K. S. Novoselov, A. K. Geim, S. V. Morozov, D. Jiang, Y. Zhang, S. V. Dubonos, I. V. Grigorieva, A. A. Firsov, *Science* **306** (2004) 666–669.
2. M. J. Allen, V. C. Tung, R. B. Kaner, *Chem. Rev.* **110** (2010) 132–145.
3. S. K. Gupta, H. R. Soni, P. K. Jha, *AIP Adv.* **3** (2013) 032117–032132.
4. D. Bera, L. Qian, TK Tseng, P. H. Holloway, *Materials* **3** (2010) 2260–2345.
5. J. Lu, P. Shan, E. Yeo, C. K. Gan, P. Wu, K. P. Loh, *Nat. Nanotechnol*. **6** (2011) 247–252.
6. H. Sun, L. Wu, W. Wei, X. Qu, *Mater. Today* **16** (2013) 433–442.
7. S. Zhu, S. Tang, J. Zhang, B. Yang, *Chem. Commun.* **48** (2012) 4527–4539.
8. Z. Zhang, J. Zhang, N. Chena, L. Qu, *Energy Environ. Sci.* **5** (2012) 8869–8890.
9. K. Sakamoto, N. Nishina, T. Enoki, JI Aihara, *J. Phys. Chem. A* **118** (2014) 3014-3025.
10. T. Wassmann, A. P. Seitsonen, A. M. Saitta, ; M. Lazzeri, F. Mauri, *J. Am. Chem. Soc.* **132** (2010) 3440-3451.
11. R. C. Haddon, *Aust. J. Chem.* **28** (1975) 2343–2351.
12. Y. Morita, S. Suzuki, K. Sato, T. Takui, *Nat. Chem.* **3** (2011) 197–204.
13. E. Clar, Polycyclic Hydrocarbons, Academic Press, New York, 1964, Vol. 1, pp. 1 –465.
14. J. Inoue, K. Fukui, T. Kubo, S. Nakazawa, K. Sato, D. Shiomi, Y. Morita, K. Yamamoto, T. Takui, K. Nakasuji, *J. Am. Chem. Soc.* **123** (2001) 12702–12703.
15. N. Pavliček, A. Mistry, Z. Majzik, N. Moll, G. Meyer, D. J. Fox, L. Gross, *Nat. Nanotechnol.* **12** (2017) 308–311.
16. Z. Bullard, E. C. Girão, J. R. Owens, W. A. Shelton, V. Meunier, *Sci. Rep.* **5** (2015) 7634-7640.
17. K. V. Raman, A. M. Kamerbeek, A. Mukherjee, N. Atodiresei, T. K. Sen, P. Lazic´, V. Caciuc, R. Michel, D. Stalke, S. K. Mandal, S. Blgel, M. Mnzenberg, J. S. Moodera, *Nature* **493** (2013) 509–513.
18. O. V. Yazyev, L. Helm, Phys. Rev. B **75** (2007) 125408–125412.
19. R. R. Nair, R. M. Sepioni, I–Ling Tsai, O. Lehtinen, J. Keinonen, A. V. Krasheninnikov, T. Thomson, A. K. Geim, I. V. Grigorieva, *Nat. Phys.* **8** (2012) 199–202.

20. K. M. McCreary, A. G. Swartz, W. Han, J. Fabian, R. K. Kawakami, *Phys. Rev. Lett.* **109** (2012) 186604–186608.
21. E. J. G. Santos, D. Snchez-Portal, A. Ayuela, *Phys. Rev. B* **81** (2010) 125433–125438.
22. H. Zhang, C. Lazo, S. Blgel, S. Heinze, Y. Mokrousov, *Phys. Rev. Lett.* **108** (2012) 056802–056806.
23. J. Hong, E. Bekyarova, P. Liang, W. A. de Heer, R. C. Haddon, S. Khizroev, *Sci. Rep*. **2** (2012) 624–629.
24. Y.-W. Son, M. L. Cohen, S. G. Louie, *Nature* **444** (2006) 347–349.
25. T. Espinosa-Ortega, I. A. Luk'yanchuk, Y. G. Rubo, *Phys. Rev. B* **87** (2013) 205434–205439.
26. M. Droth, G. Burkard, *Phys. Status Solidi RRL* **10** (2016) 75–90.
27. V. Sharma, N. Som, S. D. Dabhi, P. K. Jha, *ChemistrySelect* **3** (2018) 2390-2397.
28. C. Lee, W. Yang, R. G. Parr, *Phys. Rev. B* **37** (1988) 785–789.
29. M. J. Frisch, G. W. Truks, H. B. Schlegel, G. E. Scuseria, M. A. Robb, J. R. Cheeseman, et al. GAUSSIAN 09 (Revision C.01), Gaussian, Inc., Wallingford, CT, 2009.
30. Y. Li, Z. Jia, S. Xiao, H. Liu, Y. Li, *Nat. Commun*. **7** (2016) 11637–11647.
31. A. Frisch, A. B. Nielson, A. J. Holder, GaussView User manual, Gaussian Inc. Pittsburgh, PA 2000.
32. R. G. Pearson, *J. Org. Chem.* **54** (1989) 1423–1430.
33. R. G. Parr, R. G. Pearson, *J. Am. Chem. Soc.* **105** (1983) 7512–7516.
34. F. Boys, F. Bernardi, *Mol. Phys.* **19** (1970) 553–566.
35. J. Fernandez-Rossier, J. J. Palacios, *Phys. Rev. Lett.* **99** (2007) 177204–177207.
36. Y. Sun, Y. Zheng, H. Pan, J. Chen, W. Zhang, L. Fu, K. Zhang, N. Tang, Y. Du, *npj Quantum Materials* **2** (2017) 1-7.
37. H. P. Heiskanen, M. Manninen, J. Akola , *New J. Phys.* **10** (2008) 103015–103028.
38. W. N. Moulton, *J. Chem. Educ.* **38** (1961) 522–523.
39. D. Nafday, T. Saha-Dasgupta, *Phys. Rev. B* **88** (2013) 205422–205429.
40. H. L. Zhuang, G. P. Zheng, A. K. Soh, *Comput. Mater. Sci.* **43** (2008) 823–828.
41. Y. Wang, B. Wang, R. Huang, B. Gao, F. Kong, Q. Zhang, *Phys. E* **63** (2014) 276–282.

42. I. C. Gerber, A. V. Krasheninnikov, A. S. Foster, R. M. Nieminen, *New J. Phys*. **12** (2010) 113021.
43. H. Johll, H. C. Kang, E. S. Tok, *Phys. Rev. B* **79** (2009) 245416–245433.
44. J. Demaison, G. Wlodarczak, *Struct. Chem.* **5** (1994) 57–66.
45. K. Fukui, T. Yonezawa, H. Shingu, *J. Chem. Phys*. **20** (1952) 722–725.
46. D. C. Ghosh, J. Jana, *Curr. Sci.* **76** (1999) 570–573.
47. B. Galabov, P. Bobadova-Parvanova, *J. Phys. Chem. A* **103** (1999) 6793–6799.
48. J. S. Murray and P. Politzer, Molecular Orbital Calculations for Biological Systems, Oxford University Press, New York 1998, pp. 49–84.